PERGAMON

International Journal of Heat and Mass Transfer 42 (1999) 1863–1884

International Journal of HEAT and MASS TRANSFER

An implicit method for reconstructing dynamic three-dimensional phase boundaries under low Peclet number conditions

R.G. Keanini*

Department of Mechanical Engineering and Engineering Science, University of North Carolina at Charlotte, Charlotte, NC 28223, U.S.A.

Received 24 September 1997; in final form 3 August 1998

Abstract

This article develops an implicit inverse method for reconstructing dynamic multidimensional phase boundaries. The technique is suitable for problems having small liquid phase Peclet numbers, $Pe_r = (\hat{V}_r \hat{L}/\hat{\alpha})$, where $\hat{V}_r$ is the characteristic liquid phase velocity scale evaluated relative to the solid phase velocity scale, $\hat{L}$ is a characteristic length scale, and $\hat{\alpha}$ is a characteristic thermal diffusivity. Under these conditions, a multidimensional Stefan problem emerges. Explicit front-tracking procedures are eliminated by incorporating the latent heat effect in an effective, temperature dependent specific heat. Time-sequential reconstruction is then performed by solving a multidimensional nonlinear inverse heat conduction problem. As an illustration, evolving phase boundaries are reconstructed within moving and stationary plates subject to concentrated, high energy density heat sources. It is found that boundaries can be accurately reconstructed using either exact or noisy temperature measurements.

Nomenclature

c_p specific heat
$[\mathbf{C}]$ capacitance matrix
$e_n^{(k)}$ error measure at location k, time t_n
f dimensionless function of temperature
$\{\mathbf{f}_n\}$ force vector, time t_n
h specific enthalpy
h_t dimensionless time step
k thermal conductivity
$[\mathbf{K}]$ stiffness matrix
$\hat{L}$ length scale
$\hat{L}_{fg}$ latent heat of fusion
$[\mathbf{M}]$ mass matrix
N number of surface measurement locations
Pe Peclet number
$\mathbf{P(t)}$ heat flux parameter vector at time t
q heat flux
r radial coordinate
R solution domain radius
S_n sum of squares error at time t_n
t time
T temperature
$\{\mathbf{T}_n\}$ temperature vector, time t_n
$\mathbf{u}$ velocity
u_p plate speed
U Heaviside function
$\hat{V}$ velocity scale
x, y, z Cartesian coordinates
Y_k measured temperature at location k.

Greek symbols
α thermal diffusivity; material index
β exponent in Gaussian heat source
ε emissivity
η defined in equation (8)
ρ density
σ Stefan–Boltzmann constant
$\hat{\sigma}_d, \sigma_d$ dimensional and dimensionless temperature error
Υ Gaussian random number
ϕ_i weight function
Ω_L lower boundary

* Tel.: 001 704 547 4158; fax: 001 704 547 2352; e-mail: rkeanini@uncc.edu

0017–9310/98/$ - see front matter
PII: S0017–9310(98)00273–7

Ω_R far field boundary
Ω_u upper boundary.

Subscripts and superscripts
c specific heat
f fluid phase
i initial
k thermal conductivity
l liquidus
s solid phase; solidus
vap vaporization
0 constant coefficient
∞ ambient.

Diacritical mark
$\hat{}$ dimensional variable.

1. Introduction

Various inverse methods have been proposed for reconstructing phase change boundaries in freezing/melting materials. A viable inverse reconstruction method must incorporate some means of introducing a physical excitation into the melting/freezing material, a means of detecting the material's response to the excitation, and an accurate (direct) model relating the material's response to excitation. In order to allow reconstruction, the direct model must implicitly or explicitly incorporate the unknown boundary.

Material excitation and detection can be performed by a variety of mechanical, thermal, optical, and electromagnetic methods. For example, in thermal-based reconstruction, the excitation–response couple is typically a boundary heat flux distribution and the associated temperature field. The phase boundary is reconstructed by minimizing an error measure between measured temperatures (heat fluxes) and temperatures (heat fluxes) calculated by the direct model (see, e.g. Keanini and Desai [1]). In acoustically-based reconstruction [2], the material's response to ultrasonic excitation is measured and used in conjunction with a direct model of in-material acoustic response. The unknown boundary shape is altered until predicted model response matches the observed response. Finally, in an electromechanical or opto-mechanical approach, driven bulk wave modes within the liquid phase are sensed electronically [3] or optically. The unknown melt boundary shape, incorporated within a direct model of the pool's response, is obtained by matching the pool's observed response with model predictions. Unfortunately, in high-temperature-gradient applications (e.g., welding), refractive effects limit the utility of acoustic methods. Similarly, electro- or opto-mechanical approaches are subject to error due to excitation of higher-order wave modes.

This article describes a thermally-based method for reconstructing three-dimensional phase boundaries, applicable to problems where the liquid phase Peclet number is small. Under this condition, liquid phase conduction dominates convection and we recover the Stefan problem.

Relatively little work has been reported on solution of multidimensional inverse heat conduction problems (IHCP) involving phase change [1, 4, 5], while apparently no work has been reported on inverse solution of the three-dimensional Stefan problem. Hsu et al. [4] used embedded thermocouples within the solid phase to determine the time-varying position of a two-dimensional phase interface during the early stages of weld pool formation. Benard and Afshari [5] determined the transient position of a simulated two-dimensional phase interface based on simulated thermal measurements on an external surface. Keanini and Desai [1] reconstructed experimental, quasisteady, three-dimensional phase interfaces during analog welding experiments. (We distinguish between inverse phase change problems and inverse phase change control problems. In the former, the unknown phase interface position is determined using external and/or internal thermal data. In the latter, phase interface motion is controlled by manipulating external thermal loads. Solution of the three-dimensional inverse control problem has been reported by Alexandrou et al. [6].)

Although we will focus on solution of three-dimensional inverse phase change problems, it is important to note that the present inverse method can be directly applied to transient, nonlinear, three-dimensional inverse heat conduction problems in which phase change does not occur. As in the case of multidimensional inverse phase change problems, this problem has received relatively little attention, with existing studies focused on the linear problem [7–11]. Indeed, it appears that no work has been reported on the three-dimensional, transient, non-linear IHCP.

2. Implicit tracking of dynamic phase boundaries

Boundary reconstruction requires some means of accounting for the boundary's time-dependent location and shape. Previous studies have used front-tracking approaches, where direct solutions are confined to the solid phase, and the phase boundary is tracked from the point of incipient melting [4, 12]. Most work in this area has focused on one-dimensional inverse Stefan problems [13–15].

An alternative, implicit method, suitable for low liquid Peclet number problems, is outlined in this paper. As noted, this approach uses a conductive direct model to calculate solid and liquid phase heat transfer. By properly accounting for latent heat effects, the unknown phase boundary is determined implicitly, eliminating the need

for explicit front-tracking. We note Voller's [16] work which developed an explicit, enthalpy-based front-tracking method for solving the one-dimensional inverse control problem. The method to be developed in this article is an implicit effective capacitance approach.

3. Direct model

For generality, consider a moving material in which phase change occurs. Let the characteristic length scale be $\hat{L}$, the liquid and solid phase velocity scales be $\hat{V}_f$ and $\hat{V}_s$, and the characteristic thermal diffusivity be $\hat{\alpha}$ (evaluated at some specified reference temperature). In addition, express temperature dependent thermal conductivity and specific heat as $\hat{k}(\hat{T}) = \hat{k}_0 f_k(T)$ and $\hat{c}_p(\hat{T}) = \hat{c}_{p0} f_c(T)$, where $\hat{k}_0$ and $\hat{c}_{p0}$ are dimensional constants and f_k and f_c are dimensionless functions of temperature. Finally, define dimensionless position, time, and velocity as $(x, y, z) = (\hat{x}/\hat{L}, \hat{y}/\hat{L}, \hat{z}/\hat{L})$, $t = \hat{t}_\alpha/(\hat{L}/\hat{V}_\alpha)$ and $\mathbf{v}_\alpha = \hat{\mathbf{v}}_\alpha/\hat{V}_\alpha$, respectively, where $\alpha = \mathrm{f}$ (fluid) or s (solid). Based on these definitions, the dimensionless energy equation within each phase assumes the form

$$Pe_\alpha\left[\frac{\partial T}{\partial t_\alpha} + \mathbf{u}_\alpha \cdot \nabla T\right] = \frac{1}{f_c(T)}\nabla\cdot[f_k(T)\nabla T] \tag{1}$$

where $\mathbf{u}_\alpha$ is the velocity in phase α, $T = (\hat{T} - \hat{T}_i)/(\hat{T}_s - \hat{T}_i)$, $\hat{T}_s$ and $\hat{T}_i$ are the material's solidus and initial temperature, and $Pe_\alpha = \hat{V}_\alpha \hat{L}/\hat{\alpha}$ is the α-phase Peclet number. We have differentiated between solid and liquid phase velocities and velocity scales since these can differ by an order of magnitude or more. For convenience, length scales in both phases are assumed equal and associated thermophysical properties are expressed as composite functions of temperature. Dimensional quantities will be denoted with a caret throughout.

3.1. Conditions allowing a Stefan model approach

The approach we describe is appropriate when relative liquid phase velocities, $\hat{\mathbf{v}}'$, are small, where $\hat{\mathbf{v}}'$ represents liquid velocities evaluated relative to the moving solid phase. In particular, we require that the characteristic relative liquid velocity scale, $\hat{V}_r$, is much smaller than the characteristic solid phase velocity scale, $\hat{V}_s$:

$$\frac{\hat{V}_r}{\hat{V}_s} \ll 1. \tag{2}$$

Under these circumstances, nondimensional liquid phase velocities can be written as

$$\mathbf{v}_f = \mathbf{v}_s + \varepsilon\mathbf{v}' \tag{3}$$

where $\varepsilon = (\hat{V}_r/\hat{V}_s)$ and where $\mathbf{v}_s$ is the instantaneous solid phase velocity. In addition, we can take the liquid phase velocity scale as $\hat{V}_s$ so that $t_f = t_s$ and $Pe_f = Pe_s$. Thus, (1) assumes the following form within the liquid phase:

$$Pe_s\left[\frac{\partial T}{\partial t_s} + (\mathbf{u}_s + \varepsilon\mathbf{v}')\cdot\nabla T\right] = \frac{1}{f_c(T)}\nabla\cdot[f_k(T)\nabla T]. \tag{4}$$

From this equation, it is clear that relative fluid motion can be neglected and the problem treated as a Stefan problem when

$$\varepsilon\, Pe_s = \frac{(\hat{V}_f - \hat{V}_s)\hat{L}}{\hat{\alpha}_s} \equiv Pe_r \ll 1 \tag{5}$$

where Pe_r is the Peclet number based on the relative fluid velocity scale.

The parameter Pe_r is determined in part by the dominant body or surface force within the liquid phase, e.g., by thermocapillary, Lorentz, or buoyancy forces. For example, in the case of thermocapillary-driven flow, the appropriate velocity scale, determined by balancing free-surface thermocapillary and viscous shear stresses, is $\hat{V}_f = \hat{\sigma}_T \Delta\hat{T}\hat{l}_n/(\hat{\mu}\hat{l}_t)$, where $\hat{\sigma}_T$ is the temperature derivative of the surface tension coefficient, $\Delta\hat{T}$ is the characteristic free-surface temperature scale, and $\hat{l}_n$ and $\hat{l}_t$ are characteristic length scales in the normal and tangential directions. In this case, (5) becomes $[\hat{\sigma}_T\Delta\hat{T}\hat{l}_n/(\hat{\mu}\hat{l}_t) - \hat{V}_s]\hat{L}/\hat{\alpha}_s \ll 1$. Similar conditions can be derived for buoyancy and Lorentz-driven flows.

4. Example: weld pool evolution

In order to illustrate the approach and maintain somewhat reasonable inverse solution times, we will consider the early formation of weld pools within stationary and steadily translating workpieces. Our objective is two-fold. First, we would like to develop a fairly realistic numerical simulation of early weld pool development which can then be used to simulate experimental temperature data as well as experimental phase boundaries (where the latter will be used to assess boundary reconstruction accuracy). Second, we would like to illustrate the boundary reconstruction procedure by: (i) describing surface heat flux parameterization, (ii) the direct heat transfer model used in the reconstruction code, and (iii) operation of the implicit reconstruction algorithm. The reconstruction code will be used to estimate time-varying three-dimensional phase boundary shapes as well as the time-dependent top-side heat flux distribution. A wide range of alternative problems in crystal growth, glass processing, cryopreservation, casting, concrete setting, micro- and nano-scale fabrication, etc., could be usefully treated. With respect to welding, alternative problems could include transient reconstruction of spot welds or friction welds.

4.1. Welding simulation problem definition

We will assume that the workpiece is heated by a high power density Gaussian heat source, simulating laser or focused plasma arc heating. A coordinate system is fixed at a point immediately below the heat source, as shown in Fig. 1. The problem is assumed to be symmetric with respect to the line of travel (x-axis) and early time solutions are obtained over a cylindrical subvolume within the workpiece (Fig. 1).

The boundary conditions and initial condition are as follows. On the far field boundary $\delta\Omega_R$ ($r = R$) the temperature remains at ambient

$$T = 0 \quad \text{on } \delta\Omega_R \tag{6}$$

where initial and ambient temperatures are assumed equal. In addition, a symmetry condition is applied along the x-axis:

$$\frac{\partial T}{\partial y} = 0 \quad \text{on } y = 0. \tag{7}$$

The upper surface ($\delta\Omega_u$) is heated by an external source and, once melting begins, is subject to heat loss by vaporization:

$$\frac{\partial T}{\partial z} = q_s(r,t) \quad \text{on } \delta\Omega_u \tag{8}$$

where

$$q_s(r,t) = -q_0 \exp(-\beta r^2) + q_{vap}(r,t) \tag{9}$$

$$q_0 = \hat{q}_0 \frac{\hat{L}}{(\hat{k}_0 f_k \Delta\hat{T})} \tag{10}$$

$$q_{vap}(r,t) = \frac{A\hat{L}_{fg}}{(\hat{k}_0 f_k \Delta\hat{T})} \hat{T}^{-1/2} 10^{-\eta(\hat{T})} \tag{11}$$

$$\eta(\hat{T}) = \frac{\hat{B}}{\hat{T}} \tag{12}$$

$$\Delta\hat{T} = \hat{T}_s - \hat{T}_i \tag{13}$$

$$\beta = \hat{\beta}\hat{L}^2. \tag{14}$$

The expression for q_{vap} is based on Dushman's equation where $\hat{L}_{fg}$ is the latent heat of vaporization and $\hat{A}$ and $\hat{B}$ are constants. The lower surface ($\delta\Omega_L$) is assumed to be adiabatic,

$$\frac{\partial T}{\partial z} = 0 \quad \text{on } \delta\Delta_L \tag{15}$$

and, as mentioned, the workpiece is initially in thermal equilibrium with its surroundings:

$$T = 0 \quad t = 0. \tag{16}$$

A straightforward scaling argument can be used to show that the conditions in (8) and (15) are sufficiently accurate, i.e., that radiative and convective flux components can be safely neglected. The convective and net radiative fluxes are given by:

$$\hat{q}_c = \hat{h}_c(\hat{T} - \hat{T}_\infty) \tag{17}$$

and

$$\hat{q}_r = \hat{\varepsilon}\hat{\sigma}[\hat{T}^4 - \hat{T}_\infty^4] \tag{18}$$

where $\hat{h}_c$ is the convective heat transfer coefficient, $\hat{\varepsilon}$ is the emissivity, and $\hat{\sigma}$ is the Stefan–Boltzmann constant. Estimating $\hat{h}_c$ as $\hat{h}_c \sim 10^2$, W m^{-2} K^{-1} (see, e.g., Bejan [17]), $\hat{\varepsilon} \sim 1$, $\hat{T} \sim 10^3$ K [18], and $(\hat{T} - \hat{T}_\infty) = 10^3$ K, and comparing approximate radiant and convective fluxes against the imposed area-averaged heat flux, $\bar{\hat{q}}$, we obtain

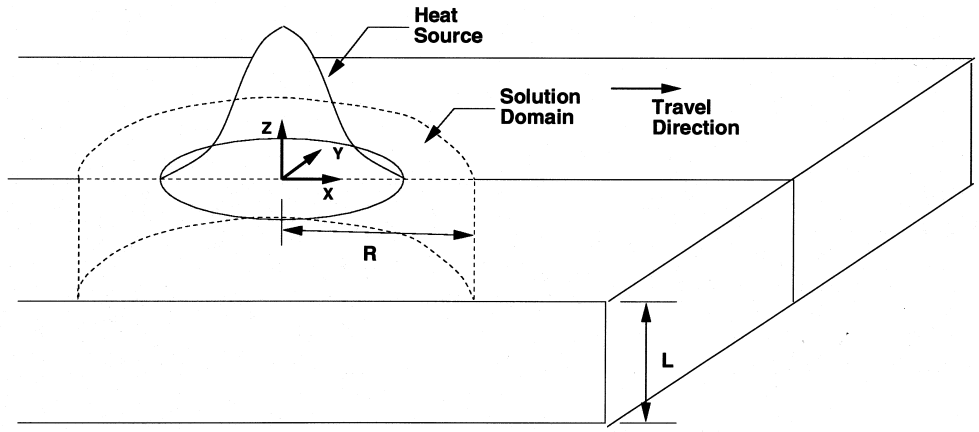

Fig. 1. Schematic of the example welding problem. Direct calculations are limited to the half-cylindrical volume within the dashed lines.

$$\frac{\varepsilon\sigma(\hat{T}^4-\hat{T}_\infty^4)}{\bar{q}} \sim 10^{-2} \tag{19}$$

$$\frac{\hat{h}(\hat{T}-\hat{T}_\infty)}{\bar{q}} \sim 10^{-1} \tag{20}$$

where $\bar{q}$ is given by

$$\bar{q} = \frac{2\hat{q}_0}{R^2\beta}[1-\exp(-\beta R^2)]. \tag{21}$$

(Based on the parameter values given immediately below, $\bar{q} = 2.77\times10^6$ W m^{-2}.) Thus, the simplified conditions in equations (8) and (15) introduce little error.

Thermophysical properties for low-carbon steel, applicable to both liquid and solid phases, are taken from Macqueene et al. [19]:

$$\hat{k}(\hat{T}) = 77.634-0.0458\hat{T} \quad \hat{T} < 1300 \text{ K} \tag{22}$$

$$\hat{k}(\hat{T}) = 30.0 \quad \hat{T} \geqslant 1300 \text{ K} \tag{23}$$

$$\hat{c}_p(\hat{T}) = 253.91+0.558\hat{T} \quad \hat{T} < 775 \text{ K} \tag{24}$$

$$\hat{c}_p(\hat{T}) = 685.6+\frac{\hat{L}}{(\hat{T}_l-\hat{T}_s)}\cdot[U(\hat{T}-\hat{T}_s)-U(\hat{T}-\hat{T}_l)] \quad \hat{T} \geqslant 775 \text{ K} \tag{25}$$

where the units on $\hat{k}$ and $\hat{c}_p$ are W m^{-1} K^{-1} and J kg^{-1} K^{-1}, respectively, and where $\hat{T}_s = 1783$ K and $\hat{T}_l = 1797$ K. Density is specified as $\hat{\rho} = 7250$ kg m^{-3} [19].

It is important to note that latent heat effects are incorporated using an effective capacitance method [19, 20] [refer to (25)]. As an alternative, enthalpy-based methods [20] could also be used. Importantly, these approaches eliminate explicit front tracking procedures by treating the solid and liquid phases as a single composite phase. The effective capacitance approach is somewhat less robust than enthalpy-based methods since nodal temperatures and energy budgets near the phase boundary are subject to error when time-dependent temperature changes become too large [20]. Here we eliminate this pathology by introducing small (fixed) time steps and by monitoring nodal temperature changes.

An effective thermal conductivity, given by equations (22) and (23), is used to account for heat transfer within the liquid phase [19]. Under low liquid phase Peclet number conditions this approach is valid, and indeed constitutes ones of the more attractive features of the reconstruction method described below. Given accurate data on the liquid phase effective thermal conductivity and given low Peclet number conditions, simulated temperature data generated using an effective thermal conductivity will be essentially identical to data obtained from numerical solution of the liquid phase flow field.

It is also important to note that early weld pool formation likely satisfies the low-Peclet number constraint. Kanouff and Grief's [21] careful simulations of stationary gas tungsten arc welding clearly show that convection (due to Marangoni, Lorentz and buoyancy forces) plays a negligible role while conduction plays a dominant role in determining early-time weld pool shapes. (For negative $\hat{\sigma}_T$, and over heating intervals of up to ten seconds, Kanouff and Greif show that time-varying pool depths, widths, and maximum temperatures are all essentially determined by conduction.)

In addition to the values listed above, the following parameter values are introduced in all calculations: $\hat{L} = \hat{R} = 5\times10^{-3}$ m, $\hat{q}_0 = 10^8$ W m^{-2}, $\hat{\beta} = 3\times10^6$ m^{-2}, $\hat{T}_i = \hat{T}_\infty = 298$ K, $\hat{L}_{fg} = 7.365\times10^6$ J kg^{-1} $\hat{A} = 2.52$, and $\hat{B} = 1.8732\times10^4$ K. Note, due to lack of equivalent data for low carbon steel, the values of $\hat{L}_{fg}$, $\hat{A}$, and $\hat{B}$ are those for stainless steel [21].

5. Numerical methods

The problem defined in the last section is solved using the Galerkin finite element method and implicit time stepping. The resulting system of equations is given by:

$$[[\mathbf{M}]+\gamma h_t([\mathbf{C}]+[\mathbf{K}])]\{\mathbf{T}_{n+1}\} = [[\mathbf{M}]-h_t(1-\gamma)([\mathbf{C}]+[\mathbf{K}])]\{\mathbf{T}_n\}+h_t\gamma\{\tilde{\mathbf{f}}_{n+1}\}+h_t(1-\gamma)\{\tilde{\mathbf{f}}_n\} \tag{26}$$

where subscripts denote the time index and where elements of the matrices [**M**], [**C**] and [**K**] are given by

$$M_{ij} = Pe_s\int_{V_e}\phi_i\phi_j\,dV \tag{27}$$

$$C_{ij} = Pe_s u_p\int_{V_e}\phi_i\phi_{j,1}\,dV \tag{28}$$

$$K_{ij} = \frac{1}{f_c(T_n)}\int_{V_e}f_k(T_n)\phi_{i,\alpha}\phi_{j,\alpha}\,dV. \tag{29}$$

Here, h_t is the dimensionless time step, γ is a constant having magnitude between 0 and 1 ($\gamma = 1$ here), and V_e is the element volume. Suppressing the time index, force vector elements are given by

$$\tilde{f}_i = \frac{1}{f_c}\int_{S_e}\phi_i q\,dS \tag{30}$$

where $q = \tilde{f}_k\nabla T\cdot\mathbf{n}$ is the dimensionless time-dependent heat flux and S_e is the element surface. Note that at time t_{n+1}, due to the use of small time steps, the temperature-dependent coefficients f_c and f_k, and the evaporative heat flux q_{vap} are evaluated using temperatures determined at time t_n.

As shown in Fig. 2, the solution domain is discretized using a combination of six-node linear triangular prism elements and eight-node linear brick elements. Mesh convergence tests indicate that the mesh shown provides sufficient solution accuracy while maintaining reasonable

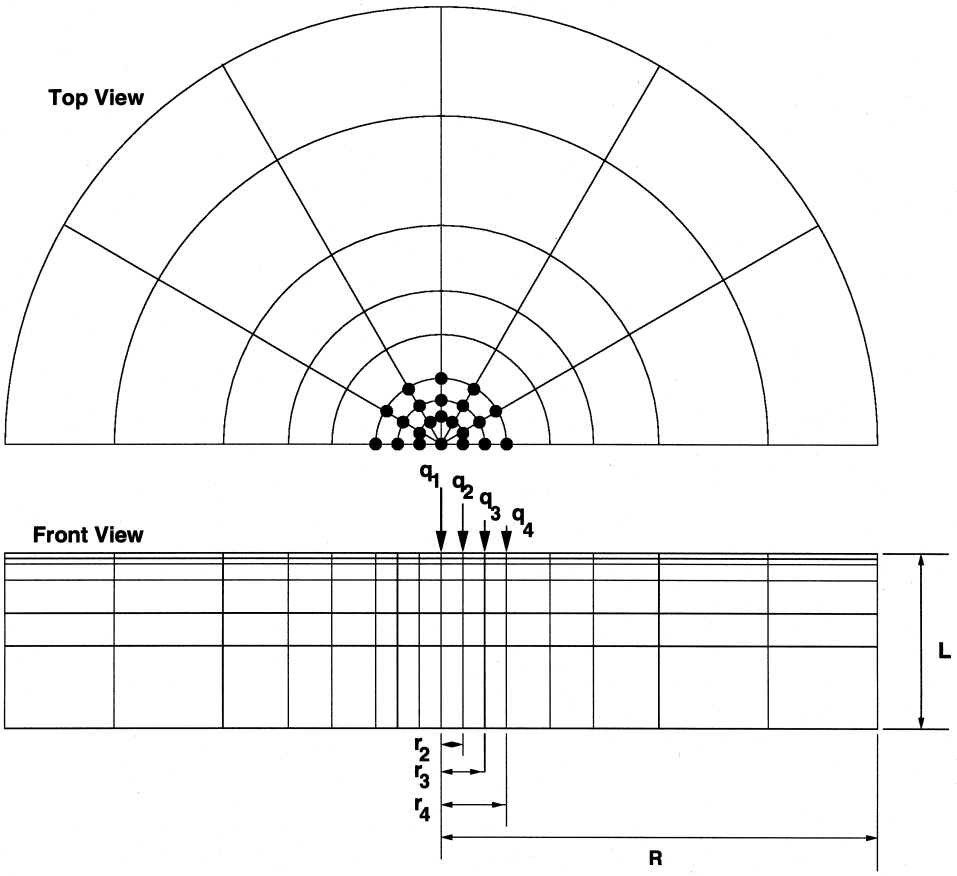

Fig. 2. Schematic showing the finite element mesh and the flux parameters determined by the inverse procedure.

direct solution costs. To ensure the validity of equation (6), the total solution time $\hat{\tau}$ is chosen to satisfy the inequality

$$\hat{u}_p\hat{\tau}+(\hat{\alpha}\hat{\tau})^{1/2} \ll \hat{R} \tag{31}$$

i.e., the time is chosen short enough that the characteristic conduction penetration depth plus the total linear displacement are significantly smaller than the solution domain's outer radius.

5.1. Data generation

As described below, the reconstruction algorithm minimizes an objective, S, which depends on a limited amount of thermal data. Here, we assume that the thermal data at time t_n consists of N surface temperature measurements $(Y_1(t_n), Y_2(t_n), \ldots, Y_N(t_n))$, obtained at N fixed, discrete measurement locations on the workpiece's upper surface. (See Keanini [22] for a brief review of noncontact surface temperature measurement techniques. Refer to Krause [18] for a description of a noninvasive measurement method suitable for welding applications.) Noisy data at these locations are simulated by first solving the direct problem, subject to the boundary and initial conditions given in (6)–(16). Given this solution, a random component is added to the calculated temperatures at each location:

$$Y_k(t_n) = T_k(t_n)+\sigma_d\Upsilon \quad K = 1,2,\ldots,N \tag{32}$$

where $T_k(t_n)$ is the calculated temperature at location k (at time t_n), σ_d is the dimensionless error, and Υ is a Gaussian random number. As described below, reconstruction has been carried out subject to (dimensional) errors $[\hat{\sigma}_d = \sigma_d(\hat{T}_s-\hat{T}_i)]$ of 0.0°C (exact data) and $\pm 2.78^\circ$C ($\pm 5^\circ$F).

6. Reconstruction procedures

6.1. Parameterization of top-side heat flux distribution

The set of parameters **P** determined by the inverse procedure is chosen to describe the top-side heat flux distribution. Since the top-side flux is both azimuthally

symmetric and dominant relative to all other surface heat transfer modes (refer to Section 4), it is found that the instantaneous top-side surface flux distribution can be adequately described using only four parameters:

$$\mathbf{P(t)} = [q_1(t), q_2(t), q_3(t), q_4(t)] \tag{33}$$

where the q_i's are shown schematically in Fig. 2. Thus, $q(r=0,t)=q_1(t)$, $q(r=r_2,t)=q_2(t)$, $q(r=r_3,t)=q_3(t)$, and $q(r=r_4,t)=q_4(t)$ with a linear variation in flux between adjacent parameters. Notice that a linear decrease in flux is also assumed between $r=r_4$ and $r=R$, where r_4 is the radial location of q_4. Since the characteristic magnitude of q_4 is roughly two-orders of magnitude smaller than q_1, q_2, and q_3, calculated temperatures are relatively insensitive to q_4 and to the assumed flux variation over $r_4 < r < R$.

6.2. Direct heat transfer problem

The direct problem solved by the reconstruction code replaces the top-side heat flux distribution in (9)–(14) by the parameterized distribution given in (33). The remaining boundary conditions in (6), (7) and (15), however, remain unchanged. As noted, the ambient temperature condition at $r=R$ is enforced by ensuring that R and the solution time, τ, satisfy the condition in (31). In experiments where phase boundaries are reconstructed over time intervals that violate (31), far field temperatures along $r=R$ must be determined experimentally [1, 22]. At least two approaches are possible:

(1) Introduce a graded mesh that provides fine spatial resolution near the melt interface and coarse resolution along the outer boundary. In particular, elements along $r=R$ should span the workpiece thickness so that no internal nodes are located on this boundary [22].
(2) An alternative approach, described by Hsu et al. [4], is to allow internal far-field nodes and to interpolate internal far-field nodal temperatures from measured surface temperatures. Although this latter approach may be viable in thin, highly conductive workpieces, it is not generally suitable.

6.3. Reconstruction algorithm

At each time step during the inverse procedure, the following sum of squares objective is minimized:

$$S_{n+1} = \sum_{j=1}^{N} (Y_{j,n+1} - T_{j,n+1})^2 \tag{34}$$

where $N=4$ is the number of measurement sites and n is the time index. Letting $\mathbf{P}_n$ represent the vector of nodal fluxes determined at t_n, the following procedure is used to determine $\mathbf{P}_{n+1}$:

(i) Beginning with an initial guess $\mathbf{P}^0_{n+1}$, iteratively alter $\mathbf{P}_{n+1}$, until S_{n+1} is minimized.
(ii) Identify the corresponding minimizing $\mathbf{P}_{n+1}$ as the estimated surface flux distribution at t_{n+1} and return to (i).

Minimization is performed using the conjugate gradient method. Initial guesses for $\mathbf{P}_{n+1}$ are generated by adding a random component to $\mathbf{P}_n$:

$$\mathbf{P}^0_{n+1} = \mathbf{P}_n(1+\sigma_p \Upsilon) \tag{35}$$

where σ_p is arbitrarily set equal to 0.1 and Υ is again a Gaussian random number.

7. Results and discussion

Inverse solutions have been obtained at two representative plate velocities: $\hat{u}_p = 0$ m s^{-1} and $\hat{u}_p = 2.5\times10^{-3}$ m s^{-1}. In order to ensure the validity of condition (6) and to maintain somewhat reasonable inverse solution times, the total solution time is limited to 0.27 s. This interval is limited since inverse solutions require on the order of eighty to one hundred cpu-hours on a Sun Sparc 20 workstation.

In the following, inverse solutions will be evaluated using the following error measure:

$$e_n^{(k)} = \frac{|\tilde{q}^{(k)}(t_n) - q_s^{(k)}(t_n)|}{q_s^{(k)}}$$
$$k = 1,2,3,4 \quad n = 1,2,\ldots,N_t \tag{36}$$

where N_t is the number of time steps comprising the solution interval, $\tilde{q}^{(k)}(t_n)$ is the estimated magnitude of the kth flux parameter at time t_n, and $q_s^{(k)}$ is the corresponding actual flux [from (9)]. The errors in (36) are evaluated at the four locations indicated by arrows (labeled by $\mathbf{q}_1$–$\mathbf{q}_4$) in Fig. 2. Since local evaporative losses at r_2, r_3, and r_4 are less than five percent of the corresponding local incoming flux, then the net flux distribution remains essentially independent of azimuthal position. Thus, the measure in (36) indicates the estimation error over the entire top surface. [Note, $N_t = 90$ and $h_t = 3\times10^{-3}$.] When comparing boundary shapes, we will refer to boundaries calculated by the direct solver as 'actual' boundaries and boundaries determined by the inverse code as 'reconstructed' boundaries.

7.1. Reconstructed boundary shapes: moving plate

Here, the plate is given as constant translation velocity of 2.5×10^{-3} m s^{-1} in the positive x-direction. Given exact data ($\hat{\sigma}_d = 0^\circ$C), the inverse code estimates the top-side flux distribution with acceptable accuracy; as shown in Fig. 3, the errors $e_n^{(2)}$, $e_n^{(3)}$, and $e_n^{(4)}$ remain below five percent essentially throughout the solution period. The

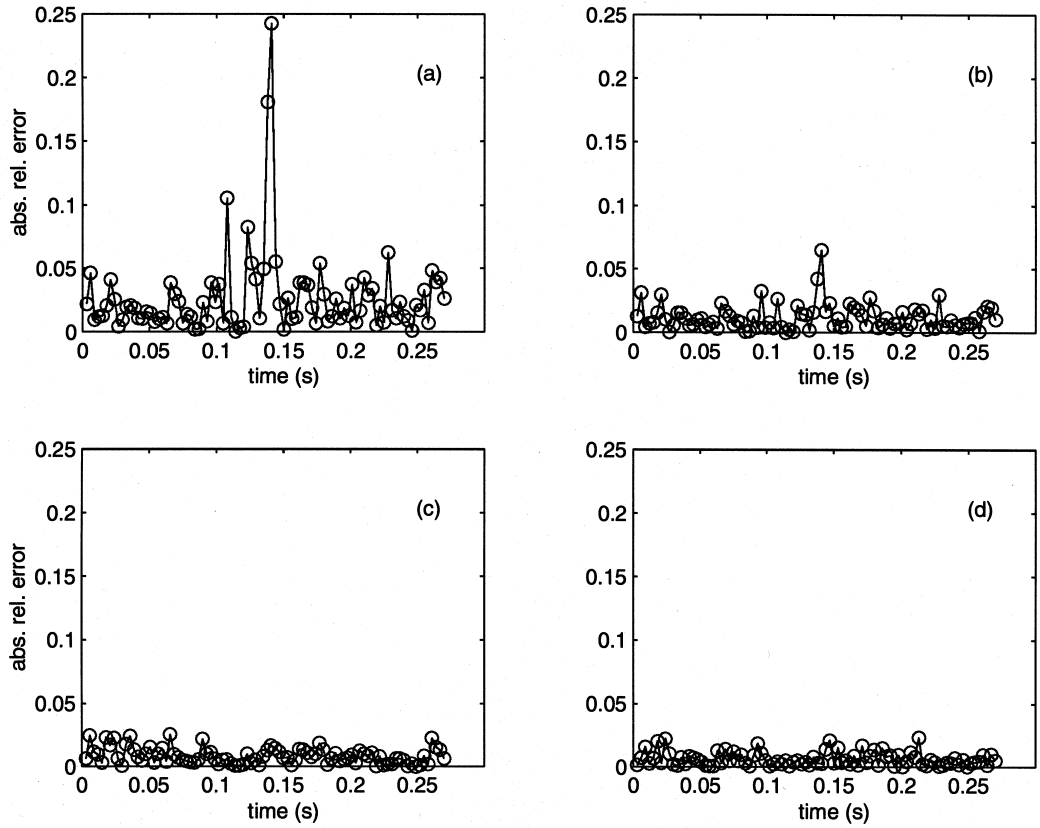

Fig. 3. Estimation errors $e_n^{(k)}$ for the four flux parameters (a) q_1, (b) q_2, (c) q_3, and (d) q_4, based on exact temperature data. The plate travel speed is $|u_s| = 2.5 \times 10^{-3}$ m s^{-1}.

error $e_n^{(1)}$ however, becomes relatively large near $\hat{t} = 1.6$ s. This apparently reflects an instability, which can be reduced somewhat through first-order regularization (result not shown). Although not attempted, the instability might also be reduced by increasing the degree of randomization σ_p in the initial parameter vector $\mathbf{P}_{n+1}^0$ [see (31)]. This strategy, which allows the minimization algorithm to sample a larger portion of the parameter space, has proven useful in earlier work [1]. Importantly, a comparison of the time-dependent reconstructed phase boundary (corresponding to $\hat{\sigma}_d = 0°C$) with the actual boundary indicates no visible differences between the two (results not shown).

When measurements are subject to errors of $\pm 2.77°C$, estimation errors $e_n^{(2)}$, $e_n^{(3)}$, and $e_n^{(4)}$ increase slightly (Fig. 4). In contrast, the apparent instability exhibited in $e_n^{(1)}$ is actually damped. This latter effect may be analogous to that of randomizing the initial parameter guess [see equation (35)], where, as mentioned, randomization allows sampling of a larger portion of the parameter space. Figures 5–9 compare reconstructed boundaries (corresponding to $\hat{\sigma}_d = \pm 2.77°C$) with actual boundaries at various times during the heating process. Clearly, the implicit approach provides reasonable boundary reconstruction, even though measurements are relatively noisy.

In closing this subsection, we note that the reconstruction procedure accurately predicts the pool boundary even though surface heat flux estimates are relatively inaccurate. Since estimated fluxes ($\hat{q}^{(k)}(t_n)$) tend to oscillate (from one time step to the next) about corresponding actual fluxes ($q_s^{(k)}(t_n)$), this feature may reflect temporal cancellation and diffusive smearing of the oscillating difference, $q_s^{(k)}(t_n) - \tilde{q}^{(k)}(t_n)$. Somewhat analogous behavior in one-dimensional inverse heat conduction problems is well known; see, e.g., [23]. In these cases, local interior temperatures are accurately reproduced while boundary heat flux estimates can exhibit relatively large errors. (The analogy is not perfect, however, since estimated interior temperatures in these problems are determined at temperature measurement sites, i.e., they comprise a portion of the objective function.) This interpretation is also consistent with the fact that first-order regularization tends to smooth heat flux estimates while negligibly impacting boundary reconstruction

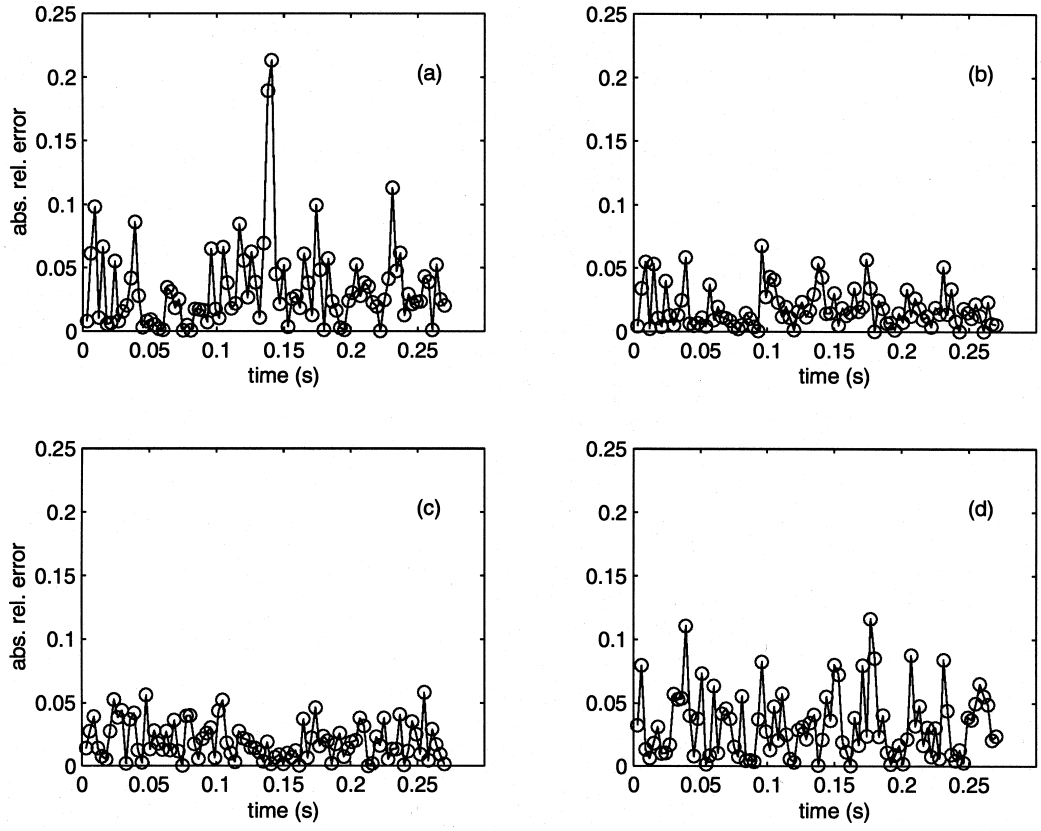

Fig. 4. Estimation errors $e_n^{(k)}$ for the four flux parameters (a) q_1, (b) q_2, (c) q_3, and (d) q_4. The plate travel speed is $|u_s| = 2.5 \times 10^{-3}$ m s^{-1} and the simulated measurement error is ± 2.77°C.

accuracy. Further work is needed to fully explore this question, however.

7.2. *Reconstructed boundary shapes: station plate*

Results similar to those observed in the last section are obtained when the plate remains stationary. For example, comparing errors in Figs 3 and 10 ($\hat{\sigma}_d = 0$°C) and in Figs 4 and 11 ($\hat{\sigma}_d = \pm 2.77$°C), we find that values of ε_1, ε_2, ε_3, and ε_4 are approximately of the same magnitude in each case. Similarly, ε_1–ε_4 generally increase when temperature measurements become noisy (see Figs 10 and 11), while ε_1 remains below 0.1 through most of both experiments (Figs 10(a) and 11(a)).

Comparison of actual and reconstructed time-varying boundary shapes in Figs 12–16 again indicate that the implicit inverse procedure provides accurate boundary reconstruction. As before, measurement uncertainty $\hat{\sigma}_d$ is ± 2.77°C. Similarly, as in the last case (where $\hat{u}_p = 2.5 \times 10^{-3}$ m s^{-1}), it is found that reconstructed boundaries associated with exact measurements ($\hat{\sigma}_d = 0$) are indistinguishable from actual boundaries (results not shown). Note, as shown in Figs 12–16, phase boundaries remain azimuthally symmetric since the heat source remains fixed relative to the plate.

In closing, we note that while the implicit reconstruction method has been illustrated using an example from welding, the method can be applied to a wide range of problems satisfying the low liquid Peclet number constraint (5). As described above, the particular form of (5) is determined by the dominant driving force within the liquid phase. We also mention that the long term goal of this work is to develop a real-time or near-real-time inverse imaging diagnostic, suitable for control and inspection applications. In order to achieve this goal, work is needed in two directions:

(1) Inverse reconstruction algorithms, suitable for unsteady, three-dimensional, moderate and high Peclet number flows are required. Many industrial liquid metal flows fall within these categories.
(2) Reconstruction using serial algorithms on single processor machines is inefficient and unsuitable for on-line process control. Significant speed-ups will likely require development of parallel reconstruction algorithms.

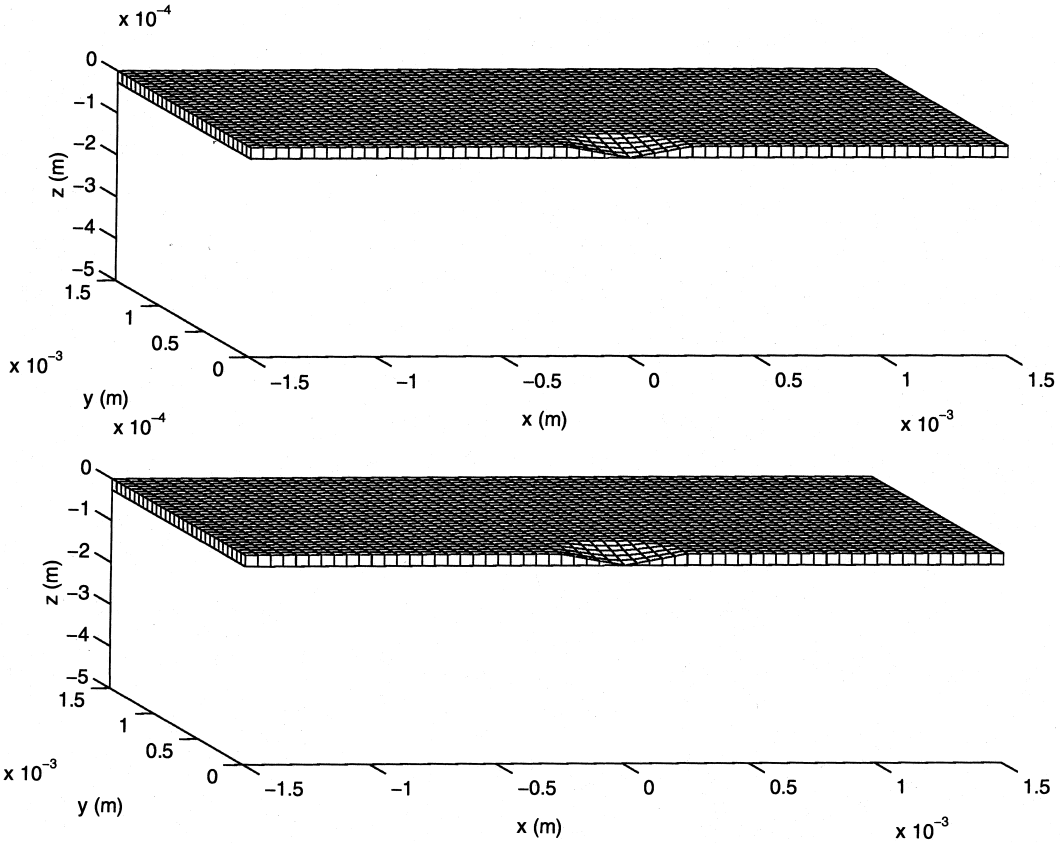

Fig. 5. Comparison of exact (upper figure) and reconstructed (lower figure) phase boundary shapes. The elapsed time since the start of heating is 0.03 s, the plate travel speed is $|u_s| = 2.5 \times 10^{-3}$ m s^{-1}, and simulated measurement error is ± 2.77°C.

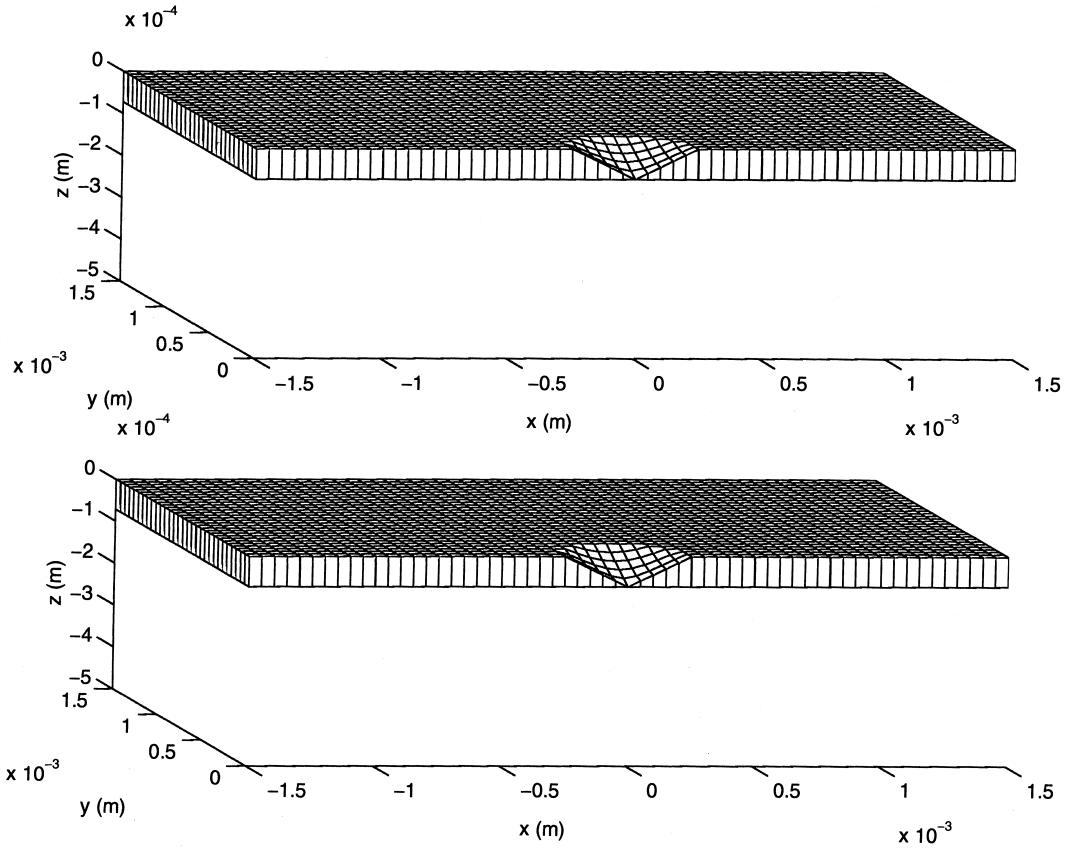

Fig. 6. Comparison of exact (upper figure) and reconstructed (lower figure) phase boundary shapes. The elapsed time since the start of heating is 0.09 s, the plate travel speed is $|u_s| = 2.5 \times 10^{-3}$ m s^{-1}, and simulated measurement error is ± 2.77°C.

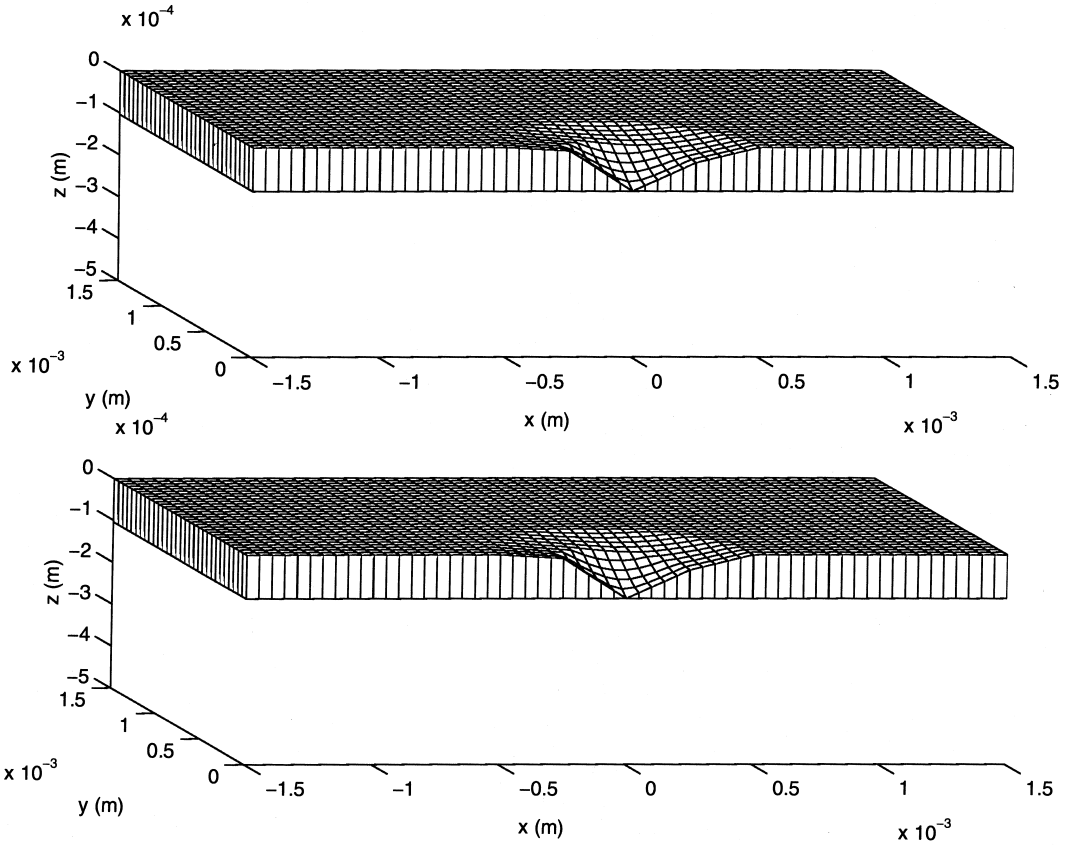

Fig. 7. Comparison of exact (upper figure) and reconstructed (lower figure) phase boundary shapes. The elapsed time since the start of heating is 0.15 s, the plate travel speed is $|u_s| = 2.5 \times 10^{-3}$ m s^{-1}, and simulated measurement error is ± 2.77°C.

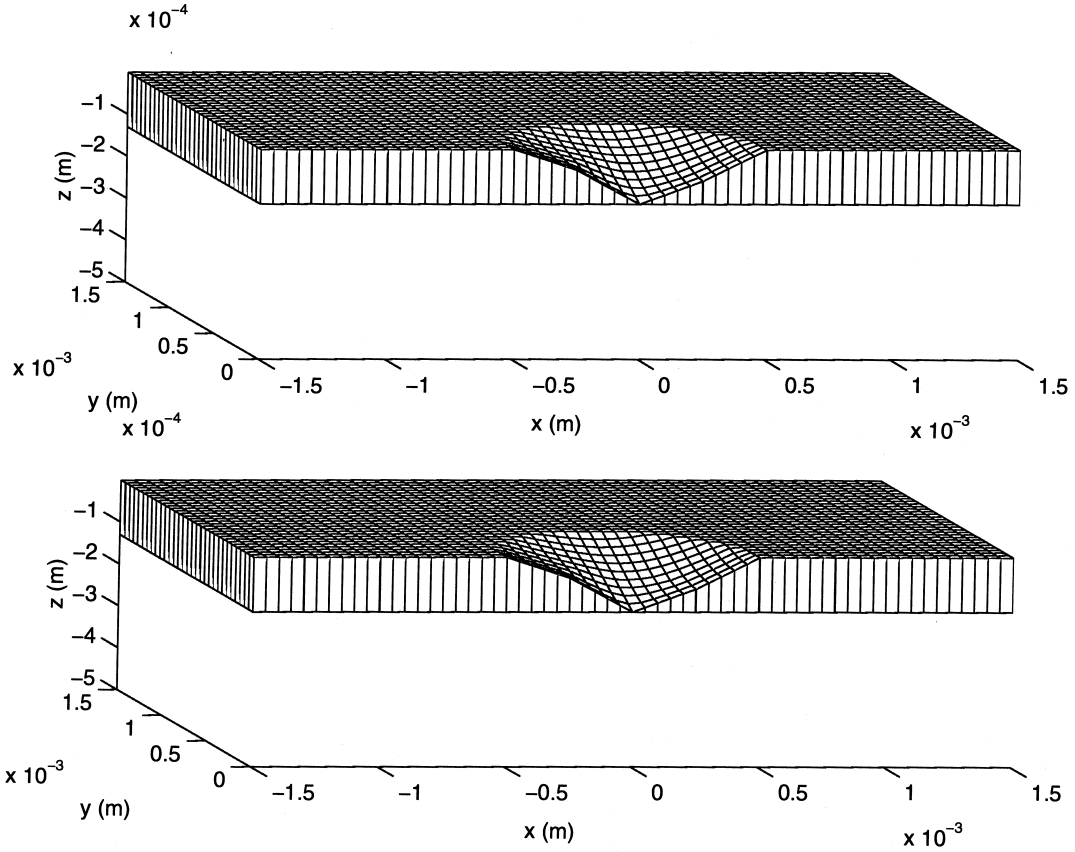

Fig. 8. Comparison of exact (upper figure) and reconstructed (lower figure) phase boundary shapes. The elapsed time since the start of heating is 0.21 s, the plate travel speed is $|u_s| = 2.5 \times 10^{-3}$ m s^{-1}, and simulated measurement error is ± 2.77°C.

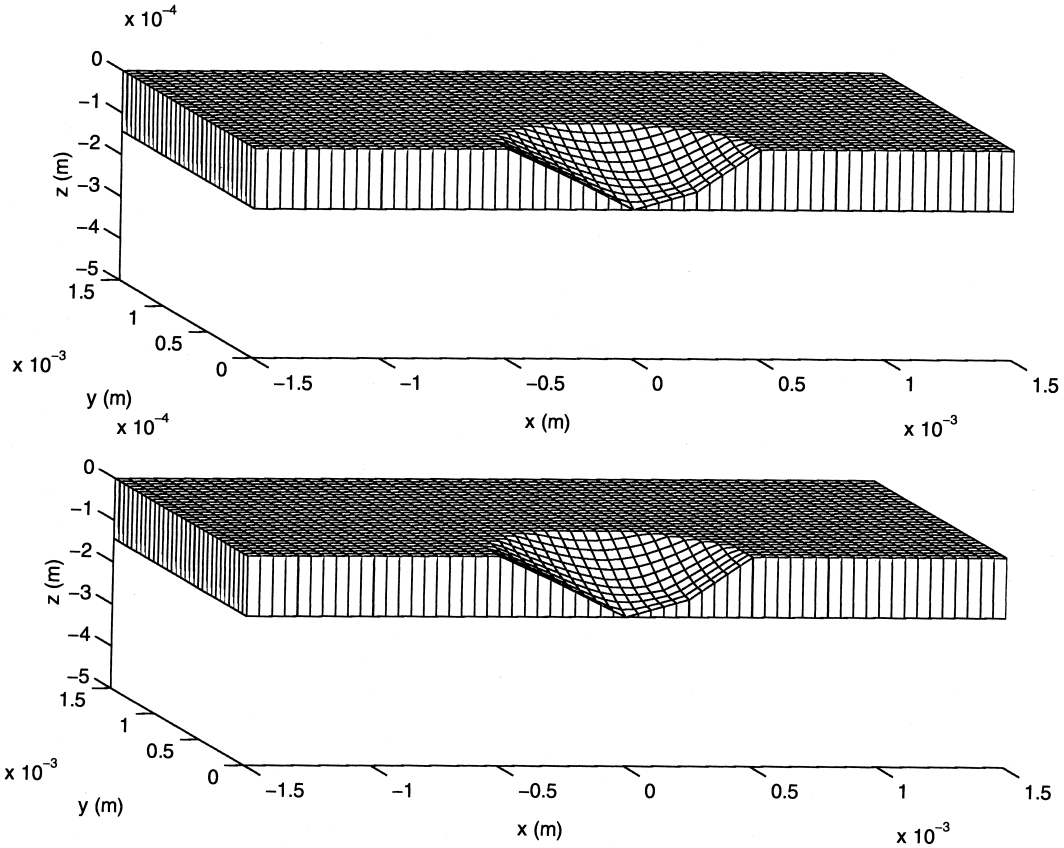

Fig. 9. Comparison of exact (upper figure) and reconstructed (lower figure) phase boundary shapes. The elapsed time since the start of heating is 0.27 s, the plate travel speed is $|u_s| = 2.5 \times 10^{-3}$ m s^{-1}, and simulated measurement error is ± 2.77°C.

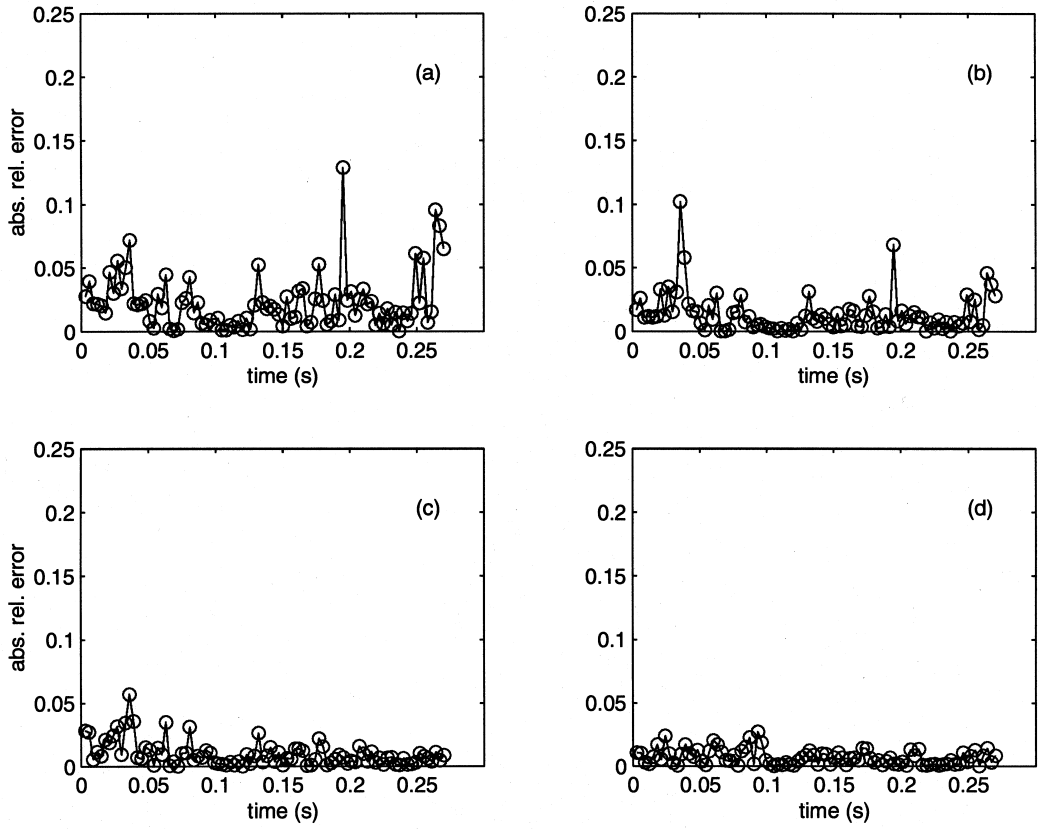

Fig. 10. Estimation errors $e_n^{(k)}$ for the four flux parameters (a) q_1, (b) q_2, (c) q_3, and (d) q_4, based on exact temperature data. The plate travel speed is stationary ($|u_s| = 0.0$ m s^{-1}).

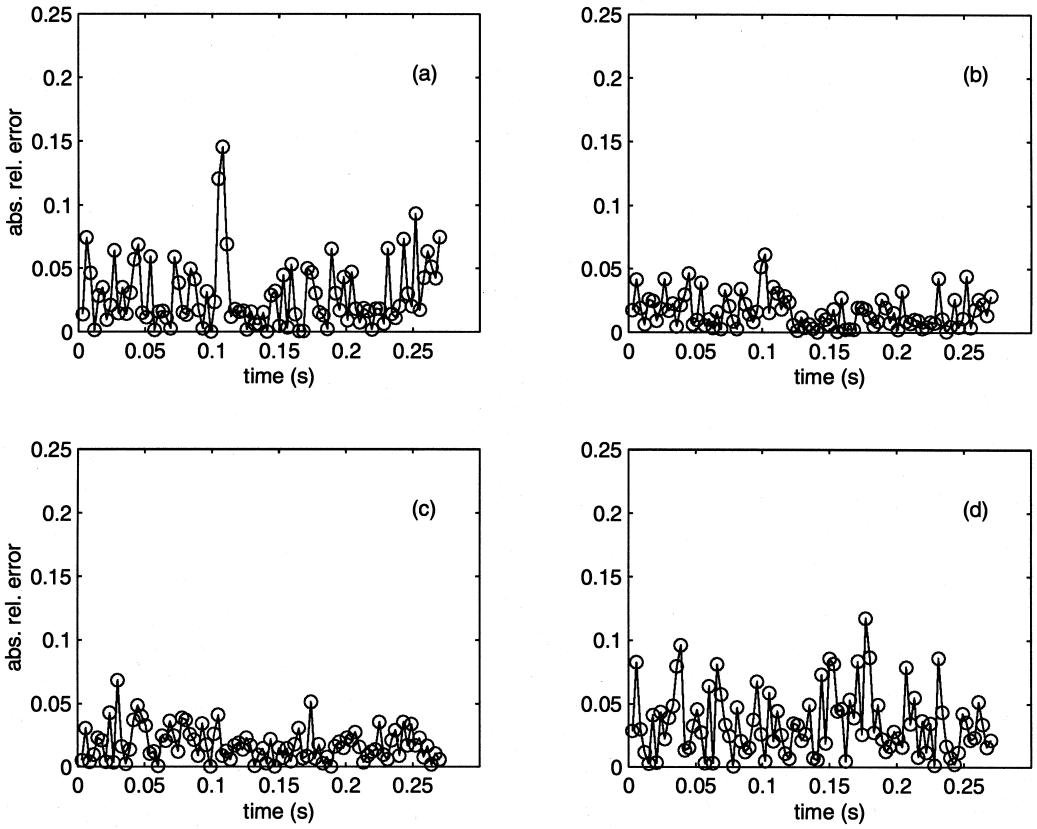

Fig. 11. Estimation errors $e_n^{(k)}$ for the four flux parameters (a) q_1, (b) q_2, (c) q_3, and (d) q_4. The plate is stationary ($|u_s| = 0.0$ m s^{-1}) and the simulated measurement error is ± 2.77°C.

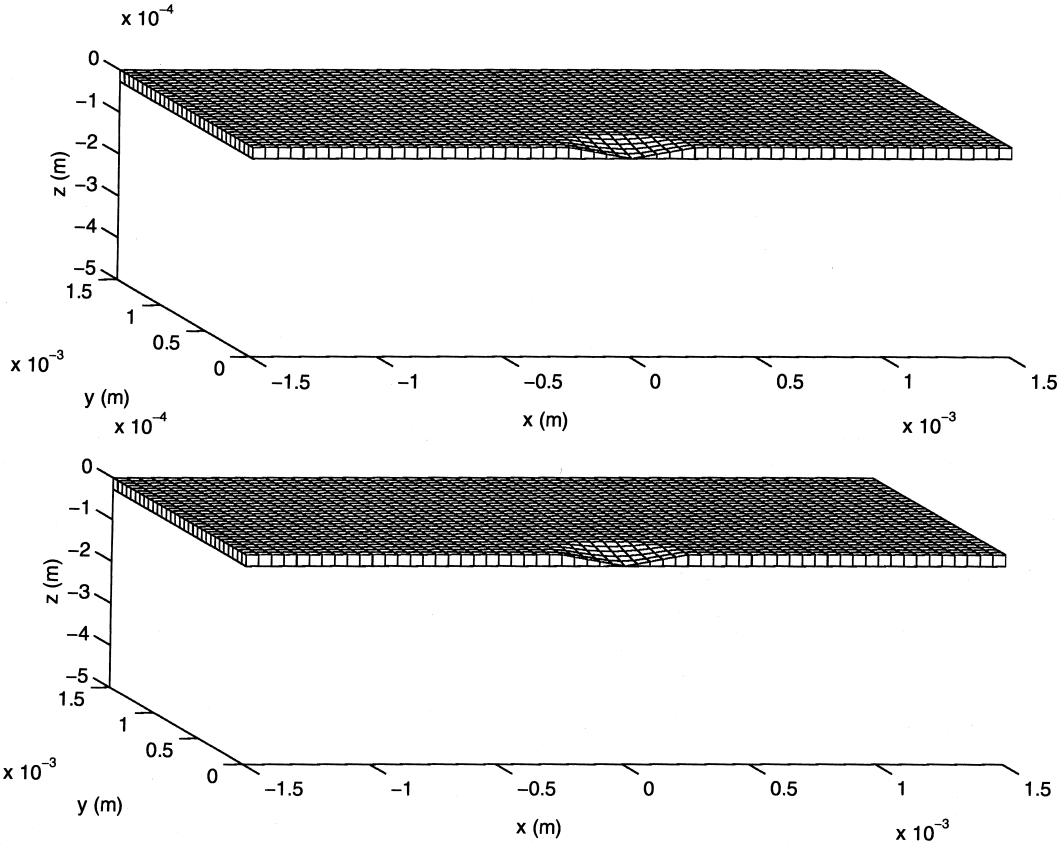

Fig. 12. Comparison of exact (upper figure) and reconstructed (lower figure) phase boundary shapes. The elapsed time since the start of heating is 0.03 s, the plate is stationary ($|u_s| = 0.0$ m s^{-1}), and the simulated measurement error is ± 2.77°C.

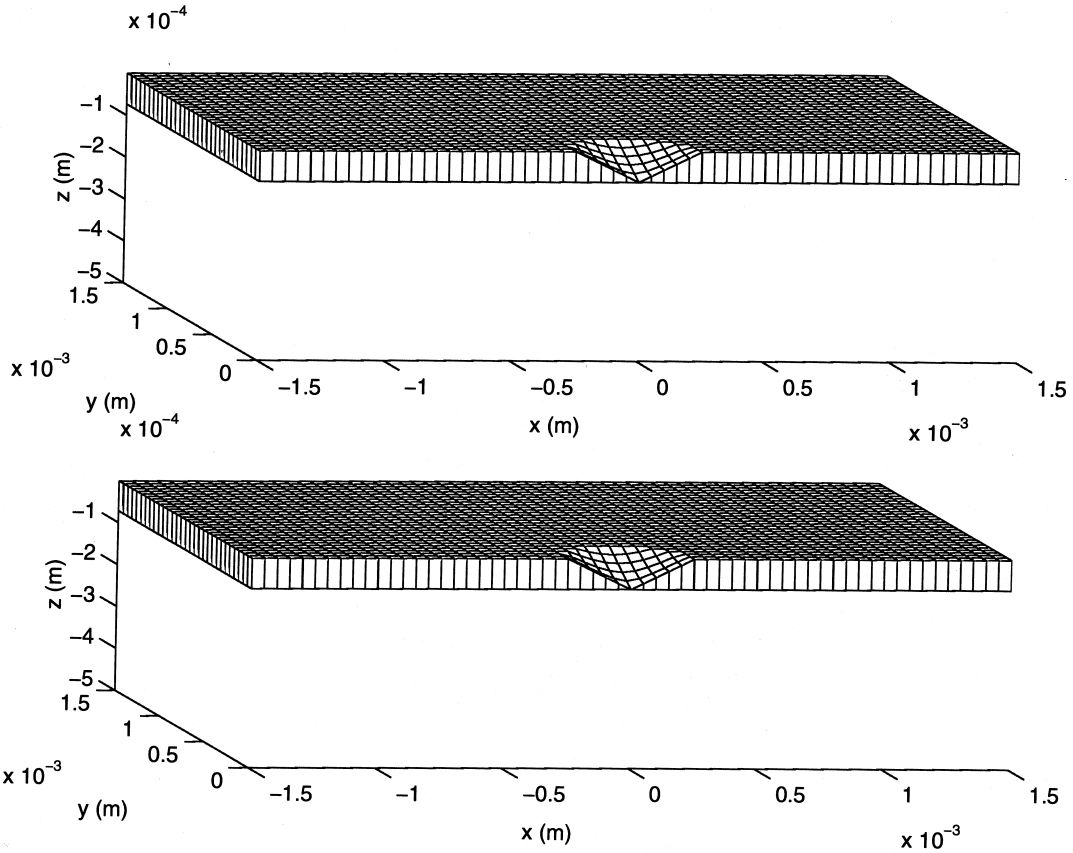

Fig. 13. Comparison of exact (upper figure) and reconstructed (lower figure) phase boundary shapes. The elapsed time since the start of heating is 0.09 s, the plate is stationary ($|u_s| = 0.0$ m s^{-1}), and the simulated measurement error is ± 2.77°C.

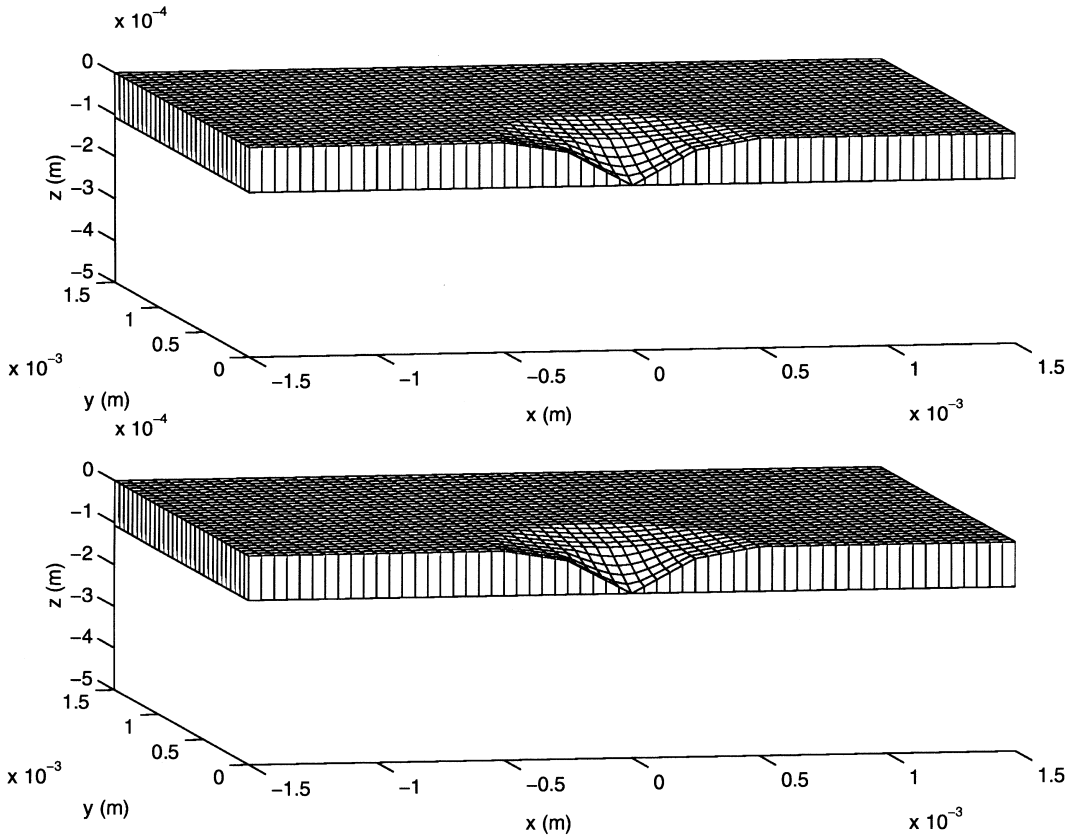

Fig. 14. Comparison of exact (upper figure) and reconstructed (lower figure) phase boundary shapes. The elapsed time since the start of heating is 0.15 s, the plate is stationary ($|u_s| = 0.0$ m s^{-1}), and the simulated measurement error is ± 2.77°C.

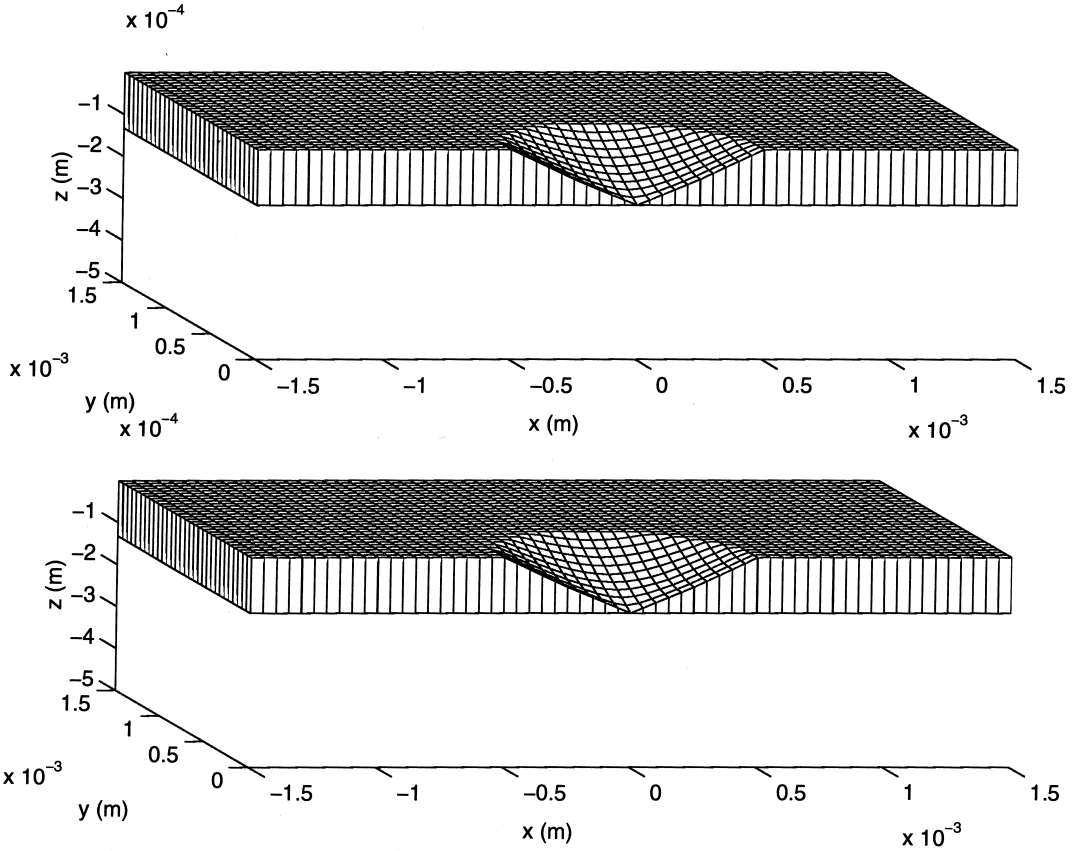

Fig. 15. Comparison of exact (upper figure) and reconstructed (lower figure) phase boundary shapes. The elapsed time since the start of heating is 0.21 s, the plate is stationary ($|u_s| = 0.0$ m s^{-1}), and the simulated measurement error is ± 2.77°C.

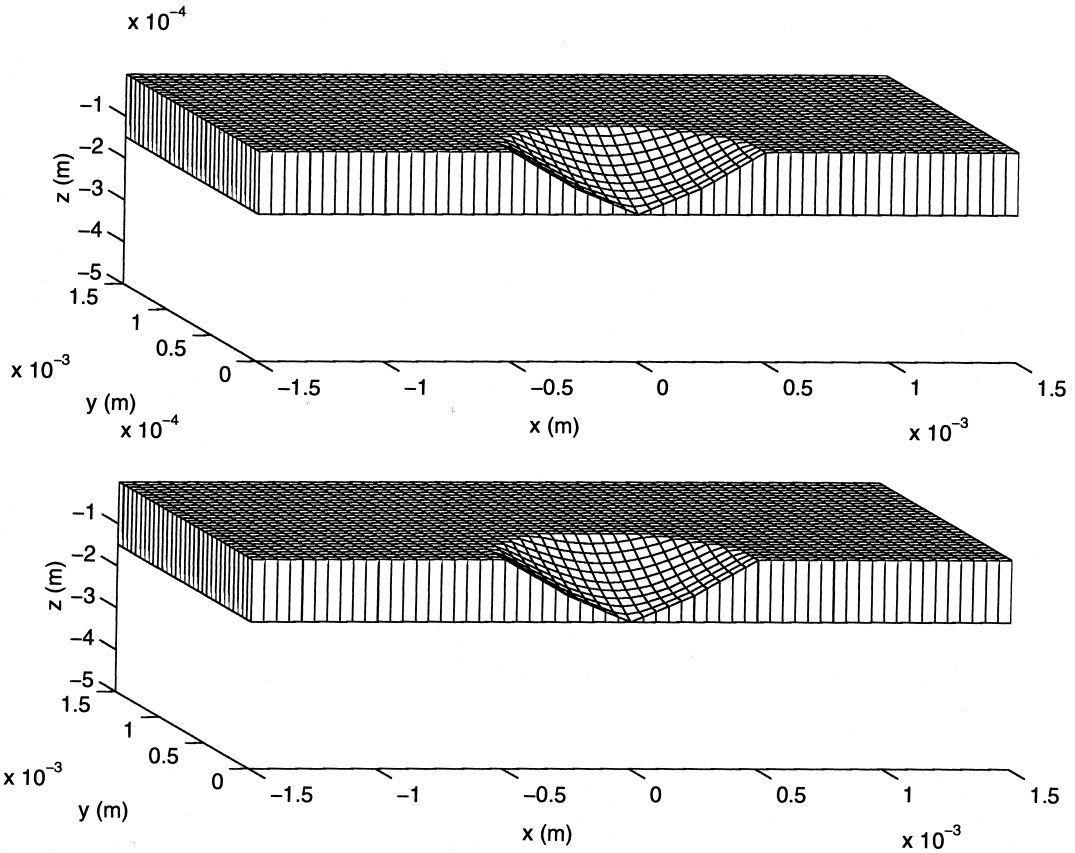

Fig. 16. Comparison of exact (upper figure) and reconstructed (lower figure) phase boundary shapes. The elapsed time since the start of heating is 0.27 s, the plate is stationary ($|u_s| = 0.0$ m s^{-1}), and the simulated measurement error is ± 2.77°C.

8. Summary and conclusions

An implicit method for reconstructing dynamic multidimensional phase boundaries has been developed. The method is suitable for problems having small liquid phase Peclet numbers. Under these conditions, a multidimensional Stefan problem emerges. Explicit front-tracking procedures are eliminated by incorporating the latent heat effect in an effective capacitance method. As an illustration, phase boundaries within moving and stationary plates, heated by concentrated, high energy density surface sources, are reconstructed. It is found that boundaries can be accurately reconstructed using either exact or noisy temperature measurements. In order to extend this work, reconstruction methods suitable for moderate and high Peclet number problems are needed. This difficult problem is under investigation.

Acknowledgements

The continued support of the Engineering Foundation is gratefully acknowledged. Special thanks to Dr Charles Freiman, Director. Additional support provided by Oak Ridge Associated Universities is also greatly appreciated.

References

[1] R. Keanini, N. Desai, Inverse finite element reduced mesh method for predicting multi-dimensional phase change boundaries and nonlinear solid phase heat transfer, International Journal of Heat and Mass Transfer 39 (1996) 1039–1049.

[2] D.E. Hardt, J. Katz, Ultrasonic measurement of weld penetration, Welding Journal 63 (1984) 273s–278s.

[3] A.S. Tam, D.E. Hardt, Weld pool impedance for pool geometry measurement: stationary and nonstationary pools, ASME Journal of Dynamics, Systems, Measurement and Control 111 (1989) 545–553.

[4] Y.F. Hsu, B. Rubinsky, K. Mahin, An inverse finite element method for the analysis of stationary arc welding processes, ASME Journal of Heat Transfer 108 (1986) 734–741.

[5] C. Benard, A. Afshari, Inverse Stefan problem: tracking of the interface position from measurements on the solid phase, International Journal of Heat and Mass Transfer 35 (1992) 835–851.

[6] A.N. Alexandrou, R. Elden, J. McConnell, An inverse approach to three-dimensional solidification problems, International Journal of Numerical Methods in Engineering 36 (1993) 135–145.
[7] N.M. Al-Najem, M.N. Ozisik, On the solution of three-dimensional inverse heat conduction in finite media, International Journal of Heat and Mass Transfer 28 (1985) 2121–2128.
[8] Y. Jarny, N. Ozisik, J.P. Bardon, A general optimization method using adjoint equation for solving multidimensional inverse heat conduction, International Journal of Heat and Mass Transfer 34 (1991) 2911–2919.
[9] A. Haji-Sheikh, F.P. Buckingham, Multidimensional inverse heat conduction using the Monte Carlo method, ASME Journal of Heat Transfer 115 (1993) 26–33.
[10] A. Haji-Shiekh, L. Yan, Multidimensional inverse heat conduction using alternative Green's function solution, International Communications in Heat and Mass Transfer 19 (1992) 661–672.
[11] D.A. Murio, H.C. Zheng, A stable algorithm for 3D-IHCP, Computers and Mathematics with Applications 29 (1995) 97–110.
[12] M. Chun, H. Choi, H. Jun, Y. Kim, Phase-change front prediction by measuring the wall temperature on which solidification occurs, International Journal of Heat and Mass Transfer 30 (1987) 2641–2650.
[13] M.A. Katz, B. Rubinsky, An inverse finite element technique to determine the change of phase interface location in one-dimensional melting problems, Numerical Heat Transfer 7 (1984) 269–283.
[14] N. Zabaras, Y. Ruan, A deforming finite element analysis of inverse Stefan problems, International Journal of Numerical Methods in Engineering 28 (1989) 295–313.
[15] N. Zabaras, Inverse finite element techniques for the analysis of solidification processes. International Journal of Numerical Methods in Engineering 29 (1990) 1569–1587.
[16] V.R. Voller, Enthalpy method for inverse Stefan problems. Numerical Heat Transfer, Part B 21 (1992) 41–55.
[17] A. Bejan, Heat Transfer, Wiley, New York, 1993, p. 24.
[18] H. Krause, Optical spectral radiometric/laser reflectance method for noninvasive measurement of weld pool surface temperatures, Optical Engineering 26 (1987) 1183–1190.
[19] J.W. Macqueene, R.L. Akau, G.W. Krutz, R.J. Schoenhals, Development of inverse finite element techniques for evaluation of measurements obtained from welding processes. Presented at the Second National Symposium on Numerical Methods in Heat Transfer, 1981, University of Maryland, College Park, MD.
[20] J.N. Reddy, D.K. Gartling, The Finite Element Method in Heat Transfer and Fluid Dynamics, CRC Press, Boca Raton, FL, 1994, pp. 17–18.
[21] M. Kanouff, R. Greif, The unsteady development of a GTA weld pool, International Journal of Heat and Mass Transfer 35 (1992) 967–979.
[22] R.G. Keanini, Review: reconstruction and control of phase boundaries during fusion welding, Trends in Heat, Mass and Momentum Transfer 3 (1997) 139–145.
[23] R.E. Johnson, R.G. Keanini, An asymptotic model of work roll heat transfer in strip rolling, International Journal of Heat and Mass Transfer 41 (1998) 871–879.